Final Draft

of the original manuscript

Yang, H.; Zander, D.; Huang, Y.; Kainer, K.; Dieringa, H.:

Individual/synergistic effects of Al and AlN on the microstructural evolution and creep resistance of Elektron21 alloy.

In: Materials Science and Engineering A. Vol. 777 (2020) 139072.

First published online by Elsevier: 08.02.2020

https://dx.doi.org/10.1016/j.msea.2020.139072

Individual/synergistic effects of Al and AlN on the microstructural evolution and creep resistance of Elektron21 alloy

Hong Yang [a]*, Daniela Zander [b], Yuanding Huang [a], Karl Ulrich Kainer [a], Hajo Dieringa [a]

[a] MagIC─ Magnesium Innovation Centre, Helmholtz-Zentrum Geesthacht, Max-Planck Straße 1, 21502, Geesthacht, Germany

[b] Chair of Corrosion and Corrosion Protection, Division of Materials Science and Engineering, RWTH Aachen University, Intzestraße 5, 52072 Aachen, Germany

* Corresponding author: hong.yang@hzg.de

Abstract

The creep properties of Mg-2.85Nd-0.92Gd-0.41Zr-0.29Zn (El21) alloys with additions of 0.25 wt.% Al, 0.75 wt.% AlN and 1 wt.% AlN/Al nanoparticles (NPs) were studied over a stress range from 80 to 140 MPa at 240 °C, respectively. The individual/synergistic roles of Al and AlN in the El21 alloy were investigated systematically to reveal their creep strengthening mechanisms. Creep results show that individually all three additions of 0.25 wt.% Al, 0.75 wt.% AlN and 1 wt.% AlN/Al could increase the creep resistance of El21 alloy apparently. However, the addition of mixed 1 wt.% AlN/Al NPs shows the best strengthening effect on creep properties in El21 alloy. Microstructural characterizations reveal that the additions of Al and AlN increased the area fraction of intermetallic particles obviously. Blocky Al_2Zr, Al_2Zr_3 particles and Al_2(Nd, Gd) (Al_2RE) particulates were observed in both El21+0.25% Al and El21+0.75%AlN. Nevertheless, when Al and AlN were simultaneously added into El21 alloy the formation of these blocky phases Al_2Zr/Al_2Zr_3 was suppressed, and a larger amount of Al_2RE phase was observed. This is attributed to the preferential reaction between AlN and Zr, which restricted the formation of Al-Zr phase and subsequently promoted the reaction of Al-RE phase. The dominant mechanism during creep at 240 °C was calculated to be viscous glide of dislocation. The simultaneous additions of Al and AlN NPs could lead to a more homogeneous distribution of intermetallic particles and increase the amount of Al_2RE phase. Such kind of microstructures is beneficial for hindering the dislocation movement, transfer the load from matrix and alleviate the local stress concentration. Consequently, El21+1% AlN/Al exhibits the best creep properties among four alloys.

Keywords: Magnesium alloys; Elektron21; Creep, Composites, High shearing

1. Introduction

Elektron21 (Mg-2.85Nd-0.92Gd-0.41Zr-0.29Zn, here named El21) alloy is a widely used commercial alloy, which was patented by Magnesium Elektron Ltd of Manchester in UK for the industrial applications in aerospace and automobile fields [1, 2]. It was specially designed with superior mechanical properties and creep resistance at room and elevated temperatures up to 200 °C together with a good castability [3]. These advantages of El21 alloy facilitate its wide applications in both civil, transportation and military industries, such as the aircraft transmission systems and the intermediate housing of engine [4].

In order to extend its applications, in recent years many scholars were attracted to further improve the properties of El21 alloy, especially with focus on its creep resistance at elevated temperatures more than 200 °C. Alloying is a commonly used method to improve the creep resistance of Mg-based alloys due to precipitation strengthening effects, such as the uses of Nd [5] and Gd [6]. These rare earth (RE) elements are relatively expensive. In addition, El21 already contains a certain amount of Nd and Gd. Further additions of REs could increase the cost of products. Therefore, the additions of external nanoparticles (NPs) to improve its strength and creep resistance have attracted much attention due to their low price. Moreover, these ceramic NPs are thermally stable. In contrast, those precipitates formed during ageing could be overaged at the application temperatures, leading to the deterioration of high temperature mechanical properties.

To date, many works have been done on the creep resistance of nanoparticle-reinforced El21 alloy. Katsarou et al. [7] selected AlN ceramic nanoparticles (NPs) containing additional nano-aluminum (Al) as reinforcements to incorporate into El21 alloy produced by an ultrasound-assisted stirring. They found that 1 wt.% AlN/Al NPs could significantly improve the creep resistance of El21 alloy under a stress range of 70-200 MPa at 240 °C. Nevertheless, the fundamental strengthening mechanisms from AlN/Al NPs on the creep resistance of El21 alloy were unraveled. Daudin et al. [8] further discussed the key roles of AlN/Al NPs on the El21 alloy based on micro- and nano-tomography techniques. They pointed out that AlN/Al NPs probably played as indirect effects on the strengthening of creep resistance in El21 alloy instead of direct effects. They speculated that Zr might be more prone to surround AlN NPs during

solidification. The individual and synergistic influence of Al and AlN NPs on the creep resistance and microstructure of El21 alloy is still unclear.

It is well know that the fabrication process to prepare Mg-based nanocomposites is of importance for the homogeneous distribution of NPs. In the last decade, ultrasonic-assisted stirring was normally applied to prepare the AlN/Al NPs reinforced El21 nanocomposites [7-10]. But unfortunately, it was verified by Saboori et al. [10] to be inadequate to homogeneously disperse the AlN/Al NPs in El21 alloy. Many discernible AlN agglomerations were observed in the matrix. Other effective manufacturing methods were therefore researched for the fabrication of El21-based composites with homogeneous distribution of reinforcements. Our previous work [11] utilized a high shearing dispersion technique (HSDT) for the first time to fabricate El21+0.5 wt.% AlN/Al composite. It was found that the creep properties of El21+0.5 wt.% AlN/Al composite was dramatically enhanced by about one order of magnitude compared to that of NP-free El21 alloy. Moreover, with HSDT preparation, the El21+0.5 wt.% AlN/Al composite shows even higher creep properties than that prepared by ultrasonic-assisted treatment, indicating HSDT is a more effective way to disperse the NPs.

It should be noticed that the previously used AlN/Al particles were a mixture of 25 wt.% Al and 75 wt.% AlN NPs [7]. When AlN and Al were simultaneously added into the El21 alloy, it is impossible to differentiate which one is mainly responsible for the enhancement of creep resistance for El21+AlN/Al composites, Al, or AlN. Our previous work [12] revealed that the pure Al addition could effectively increase the creep resistance of El21 alloy, which is attributed to the homogeneous distribution of intermetallic particles in α-Mg matrix. Unfortunately, the individual role of pure AlN NPs on the creep resistance and microstructural modification of El21 alloy still remains uncertain. Furthermore, the synergistic effects of Al and AlN NPs on the microstructural evolutions and creep resistance of El21 alloy also needs to be explored. Hence, further works are necessary to investigate the microstructural evolution and creep resistance of El21 alloy modified by Al, AlN and AlN/Al.

In this work, three key questions are raised: (1) which additive mainly contributes to the enhancement of creep properties for El21 alloy, Al or AlN NPs. (2) How does the separate/mixed additions of Al and AlN NPs influence the microstructural evolutions? (3) What is the individual/synergistic influence of Al and AlN on the creep properties of El21 alloy? In order to address these three questions, El21+0.25 wt.% Al, El21+0.75 wt.% AlN and El21+1 wt.% AlN/Al were prepared using HSDT. The unmodified-El21 alloy was also casted

following the same procedures. The microstructural evolutions with additions of Al, AlN and mixed AlN/Al in El21 alloy were systematically unraveled and compared, especially focusing on their interactions with alloying elements. The individual and/or synergistic roles in influencing the creep resistance of El21 alloy was clarified for Al and AlN.

2. Experimental procedures

The as cast commercial Elektron21 (El21) alloy, which was patented by Magnesium Elektron Ltd at Manchester, UK, was chosen as the matrix to prepare the alloy and its composites. Its chemical composition is Mg-2.85Nd-0.92Gd-0.41Zr-0.29Zn (all compositions are in wt.% unless stated) as determined using optical emission spectroscopy (OES, Spectrolab M9 Kleve, Germany) for Nd, Zr, Zn and X-ray fluorescence (XRF) analyzer (Bruker AXS S4 Explorer, Germany) for Gd element. Pure AlN nanoparticles (NPs) with a size range of 60-70 nm and a mixture of Al and AlN NPs (termed as AlN/Al NPs) with a medium size of 80 nm [13] were chosen as the reinforcements. It was confirmed by Katsarou et al. [7] that these AlN/Al nanoparticle mixtures contain 25% Al and 75% AlN NPs. Raw El21 alloys with about 12 kg were melted at 720 °C in a cylindrical mould under a protective atmosphere (Ar+2% SF_2). Then the additives of pure 0.25% Al, pure 0.75% AlN NPs and mixed 1% AlN/Al NPs were added into the melt with assistance of a high shearing dispersion technique (HSDT) at a speed of 3000 rpm for 1 min, respectively. This HSDT with a rotor-stator mixer (Φ 67.5 mm) can create a high shear stress on the melt to obtain a better distribution of the additives in the melt. Its schematic diagram and the dispersion mechanisms can be found elsewhere [14]. After intensive shearing, approximate 3 kg of the molten alloy was poured into a preheated mild steel mould (at a temperature of 450 °C) and transferred in a three-zone resistance ring furnace (ThermConcept, Bremen, Germany) for 5 min. Finally, the mould was lowed into a water bath directly underneath the furnace opening at a descending speed of 100 mm/min. For comparison, unmodified El21 alloy was also prepared using HSDT following the same procedures. Detailed casting parameters for these above four materials are listed in Table 1.

Table 1. Casting parameters and grain sizes of El21 alloy, El21+0.25% Al alloy, El21+0.75% AlN composite and El21+1% AlN/Al composite.

Materials	High-shearing speed/ rpm	High-shearing time/ min	Grain size/ μm
El21	3000	1	59.4±1.6
El21+0.25% Al	3000	1	167.0±5.7
El21+0.75% AlN	3000	1	100.0±5.2
El21+1% AlN/Al	3000	1	463.5±17.5

Compressive creep tests were carried out using an Applied Test System (ATS) lever arm creep test systems under 80, 100, 120 and 140 MPa at 240 °C, respectively. The gauge dimension of creep specimens was Φ 6×15 mm. The creep measurements were interrupted once the steady-state creep region was obtained. The microstructures were characterized using optical microscopy (OM, Reichert-Jung MeF3, USA). Average grain size was calculated by the AnalySIS Pro software (Olympus Soft Imaging Solutions, Germany) using the linear intercept methods [15]. The back scattered electron (BSE) micrographs were acquired using a scanning electron microscope (SEM, Tescan Vega3-SB, Czech Republic) equipped with an energy-dispersive X-ray spectroscopy (EDS). ImageJ software was used to calculate the area fractions for intermetallic particles based on the BSE micrographs. Phase identifications were analyzed by X-ray diffraction (XRD) with a Cu diffractometer (wave length 0.15418 nm) at 40 kV and 40 mA. The characterizations of the orientation imaging microscopy (OIM) and kernel average misorientation (KAM) were acquired using electron backscatter diffraction (EBSD) measurement at a voltage of 15 kV (Zeiss, Ultra 55). The specimens were electro-polished in AC2 solution at ~20 °C and 30 V prior to the EBSD measurements.

3. Results

3.1 Creep properties

Fig. 1 depicts the representative compressive creep curves of El21 alloy, El21+0.25% Al alloy, El21+0.75% AlN composite and El21+1% AlN/Al composite. It shows the creep strain as a function of time under the applied stresses of 80, 100, 120 and 140 MPa at 240 °C, respectively. These curves exhibit that after a relative short primary creep stage, a rather long secondary creep stage takes place. Their creep strains increase obviously with increasing the time and applied stresses. The creep strain of El21 alloy increases fastest over time under all the applied stresses, demonstrating that it has the worst creep resistance among all the materials. With the

additions of 0.25% Al and 0.75% AlN NPs in El21 alloy, their creep strains are both significantly lower than that for El21 alloy, indicating that both the additions of pure Al and AlN NPs can improve the creep resistance of El21 alloy. By adding 1% AlN/Al NPs in El21 alloy, it exhibits the lowest creep strain, indicating that it has the best creep resistance among these four materials.

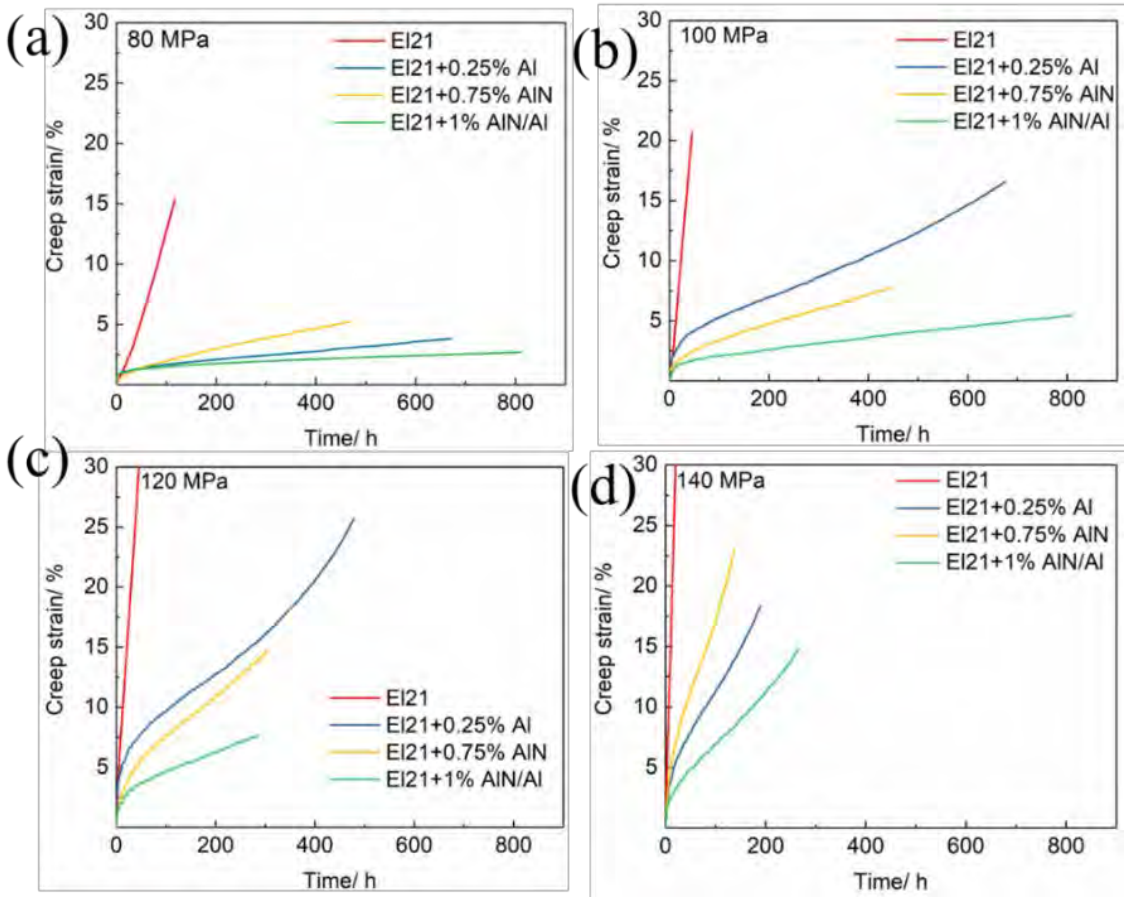

Fig. 1. Creep strain curves over time for El21 alloy, El21+0.25% Al alloy, El21+0.75% AlN composite and El21+1% AlN/Al composite at 240 °C under the stresses of (a) 80 MPa, (b) 100 MPa, (c) 120 MPa and (d) 140 MPa.

Fig. 2 shows the curves of creep rates as a function of time from which the minimum creep rate can be obtained. These curves were plotted by derivation of the creep strain with respect to the creep time. All the curves exhibit an instantaneous decrease in the creep rate at the primary creep stage at which thermal softening was less effective than working hardening [16]. Then they experienced a steady-state region at the secondary creep stage at which a relative balance occurred between work hardening and thermal softening. By adding 0.25% Al, 0.75% AlN and 1% AlN/Al NPs in El21 alloy, their minimum creep rates are distinctly less than that of El21 alloy under the same creep time. El21+0.25% Al, El21+0.75% AlN and El21+1% AlN/Al have

minimum creep rates of 2.68×10^{-7}, 4.36×10^{-7} and 1.52×10^{-7} s^{-1} at 140 MPa, respectively. They are more than one order of magnitude lower than that of El21 alloy (4.01×10^{-6} s^{-1}) (Table 2). The ratio values of $\dot{\varepsilon}$ (El21) / $\dot{\varepsilon}$(El21+*x* Al/AlN) reflect the improvement of creep resistance quantitatively. The higher ratios, the larger strengthening effects from the additives (Table 2). It can be concluded that the contributions from 0.25% Al and 0.75% AlN NPs to the creep resistance of El21 are quite similar. Both of them are much smaller than that from 1% AlN/Al NPs. Moreover, the increment of creep resistance by adding 1% AlN/Al NPs in El21 is even higher than the sum by adding individual 0.25% Al and 0.75% AlN (Table 2). This suggests that the combinative additions of 0.25% Al and 0.75% AlN in 1% AlN/Al NPs has a synergistic strengthening effect on the creep properties for El21 alloy.

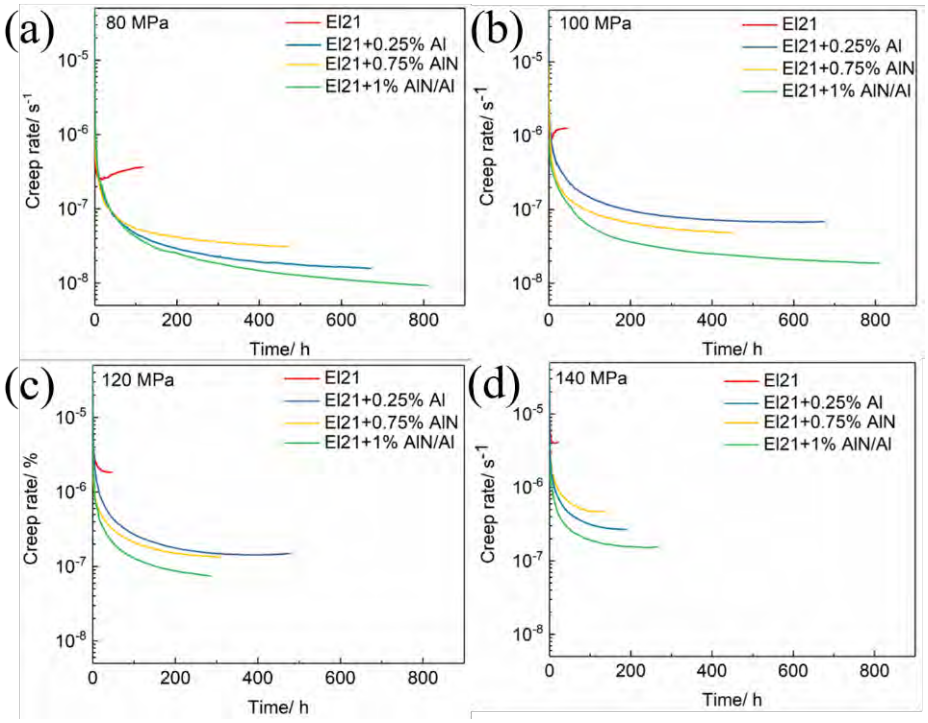

Fig. 2. Creep rates over time of El21 alloy, El21+0.25% Al alloy, El21+0.75% AlN composite and El21+1% AlN/Al composite at 240 °C under the stresses of (a) 80 MPa, (b) 100 MPa, (c) 120 MPa and (d) 140 MPa.

Table 2. Minimum creep rates under the applied stresses of 80, 100, 120 and 140 MPa at 240 °C. The ratio values (ratio=ε̇ (El21) / ε̇(El21+*x* (*x*=0.25%Al, 0.75%AlN and 1%AlN/Al)) are also listed.

No.	Materials	Stress/ MPa	$\dot{\varepsilon}$/ s^{-1}	Ratio
1	El21	80	2.5×10^{-7}	/
		100	9.25×10^{-7}	/
		120	1.83×10^{-6}	/
		140	4.01×10^{-6}	/
2	El21+0.25% Al	80	1.56×10^{-8}	16.0
		100	6.71×10^{-8}	13.8
		120	1.47×10^{-7}	12.4
		140	2.68×10^{-7}	15.0
3	El21+0.75% AlN	80	3.13×10^{-8}	8.0
		100	4.85×10^{-8}	19.1
		120	1.34×10^{-7}	13.7
		140	4.36×10^{-7}	9.2
4	El21+1% AlN/Al	80	9.05×10^{-9}	27.6
		100	1.87×10^{-8}	49.5
		120	7.36×10^{-8}	24.9
		140	1.52×10^{-7}	26.4

3.2 Optical microstructures and intermetallic morphologies

Fig. 3(a-d) shows the optical microstructures of as cast El21 alloy, El21+0.25% Al alloy, El21+0.75% AlN composite and El21+1% AlN/Al composite sheared at 3000 rpm for 1 min, respectively. El21 alloy exhibits the typical equiaxed grains with an average size of 59.4±1.6 μm (Table 1, Fig. 3(a)). With the additions of Al and AlN in El21 alloy, the grains were changed to pronounced dendritic grains. Their grain sizes increase obviously to 167.0±5.7 and 100.0±5.2 μm, respectively (Fig. 3(b-c)). By adding 1% AlN/Al NPs in El21 alloy, its grains were coarsened dramatically with an average size of 463.5±17.5 μm (Fig. 3(d)). XRD patterns indicate that the as cast El21 alloy is mainly made up of α-Mg and Mg_3(Nd, Gd) (Mg_3RE) intermetallic particles (Fig. 4(a)). Mg_3RE phase has a similar crystal structure to Mg_3Nd phase, in which parts of Nd were substituted by Gd atoms without changing the crystal structure due to their similar atomic radii [10]. With the additions of 0.25% Al and 0.75% AlN NPs, no additional phases are observed in El21+0.25% Al alloy and El21+0.75% AlN composites (Fig. 4(b-c)). Nevertheless, it cannot be concluded that no additional phases were formed by adding 0.25% Al and 0.75% AlN in El21 alloy due to their possible relatively low contents, which made them difficult to be detected by XRD. With the addition of 1% AlN/Al NPs, besides α-

Mg matrix and Mg_3RE phase, additional $Al_2(Nd, Gd)$ (Al_2RE) peaks were found in El21+1% AlN/Al composite (Fig. 4(d)).

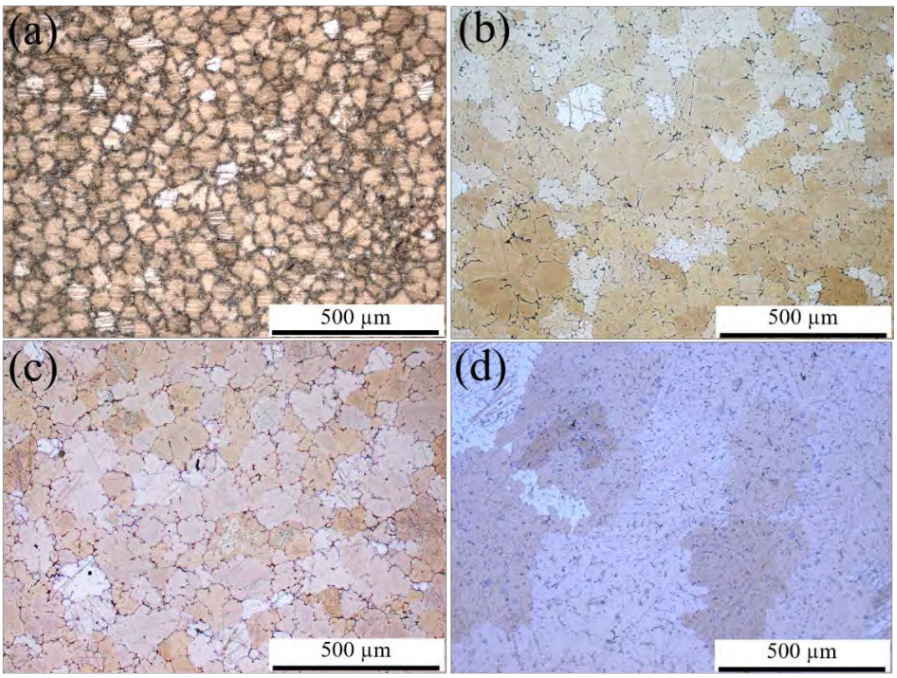

Fig. 3. Optical microstructures of as-cast (a) El21 alloy, (b) El21+0.25% Al alloy, (c) El21+0.75% AlN composite, (d) El21+1% AlN/Al composite.

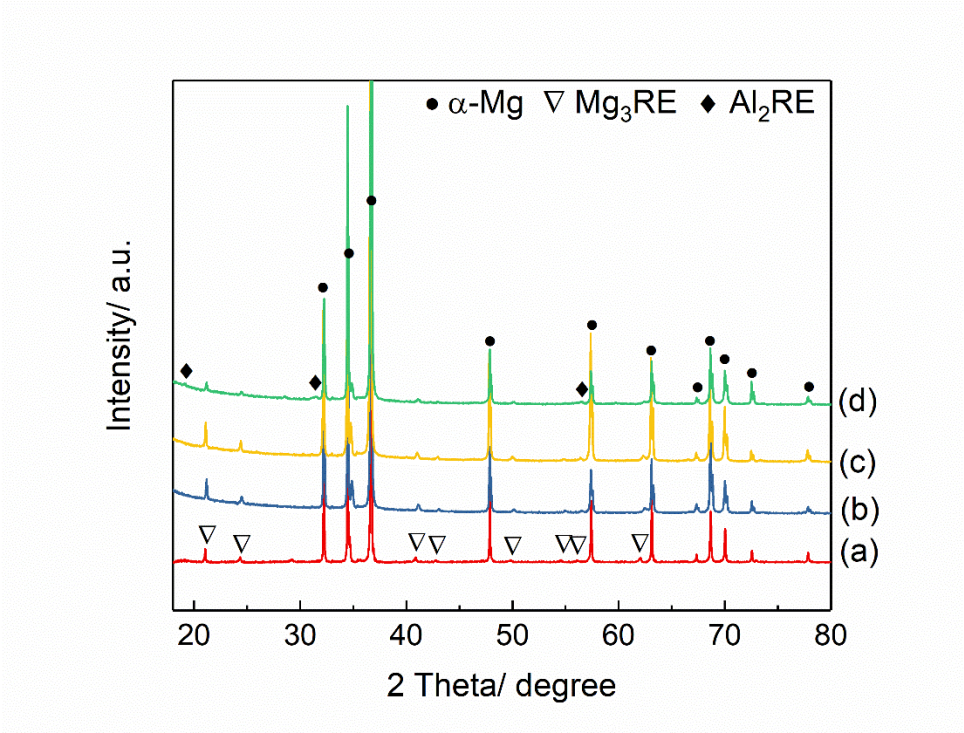

Fig. 4. XRD patterns of as-cast (a) El21 alloy, (b) El21+0.25% Al alloy, (c) El21+0.75% AlN composite, (d) El21+1% AlN/Al composite.

The BSE micrographs reveal that El21 alloy has a typical network morphology of intermetallic particles with an area fraction of 5.9% (Fig. 5(a)). It was confirmed by XRD patterns that these intermetallic particles are Mg_3RE phase. By adding 0.25% Al into El21 alloy, its intermetallic distribution obviously becomes denser with distinct dendrites (Fig. 5(b)). Similar phenomenon was also observed in El21+0.75% AlN composite (Fig. 5(c)). The dendritic morphology of intermetallic particles is more pronounced in El21+0.25% Al than that in El21+0.75% AlN, indicating that pure Al addition is more efficient than pure AlN addition to result in morphological modification of intermetallic particles in El21 alloy. In addition, the quantitative measurements indicate that the area fractions of the intermetallic particles in El21+0.25% Al alloy and El21+0.75% AlN are 12.0% and 9.0%, respectively, which are both higher than that in El21 alloy. However, their distributions of intermetallic particles in Fig. 5(b-c) are not so homogeneous as indicated by orange arrows with relatively large-sized intermetallic morphology. In El21 alloy with addition of 1% AlN/Al NPs, its grains are obviously larger than that of El21 alloy, but its intermetallic particles are much smaller and more densely distributed in the matrix. Although the area fraction of intermetallic particles in El21+1% AlN/Al composite (10.4%) is slightly lower than that of El21+0.25% Al (12.0%), its distribution is much more homogenous than that of the latter (Fig. 5(d)).

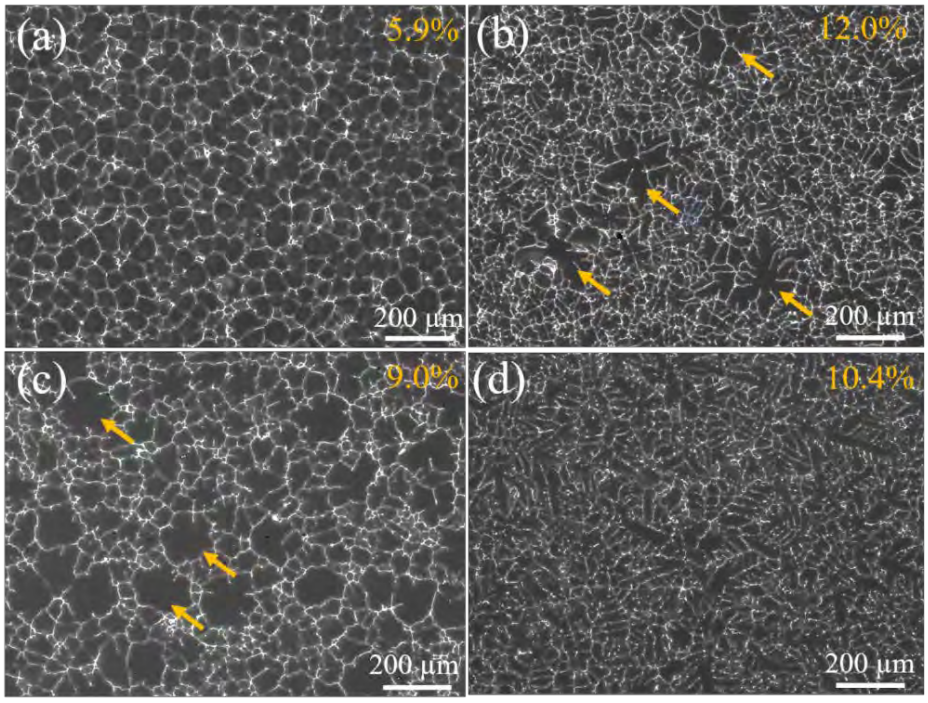

Fig. 5. BSE micrographs of as cast (a) El21 alloy, (b) El21+0.25% Al alloy, (c) El21+0.75% AlN composite, (d) El21+1% AlN/Al composite. Area fractions of intermetallic particles in

these alloys were calculated using ImageJ software. The corresponding values were inserted in (a-d), respectively.

The intermetallic morphologies of these four alloys and their magnified lamellar eutectic Mg_3RE phase are shown in Fig. 6. The Mg_3RE phase with a network morphology is mainly distributed at the grain boundaries in El21 alloy. Almost no phase can be observed inside the α-Mg matrix (Fig. 6(a)). After adding 0.25% Al, 0.75% AlN NPs and 1% AlN/Al in El21 alloy, the distribution of eutectic phases is more homogeneous than that in El21 alloy (Fig. 6(c), (e) and (g)). These eutectic phases in El21+0.25% Al, El21+0.75% AlN and El21+1% AlN/Al were not only distributed along the grain boundaries, but also at the dendritic boundaries. In addition to this, in El21 alloy, many lath-like precipitates $Mg_{12}Nd$ were formed near the Mg_3RE phase [12] (Fig. 6(b)). With the addition of 0.25% Al, 0.75% AlN and 1% AlN/Al, the formation of such $Mg_{12}Nd$ precipitates were suppressed. No obvious precipitates can be observed near the eutectic region (Fig. 6(d), (f) and (h)).

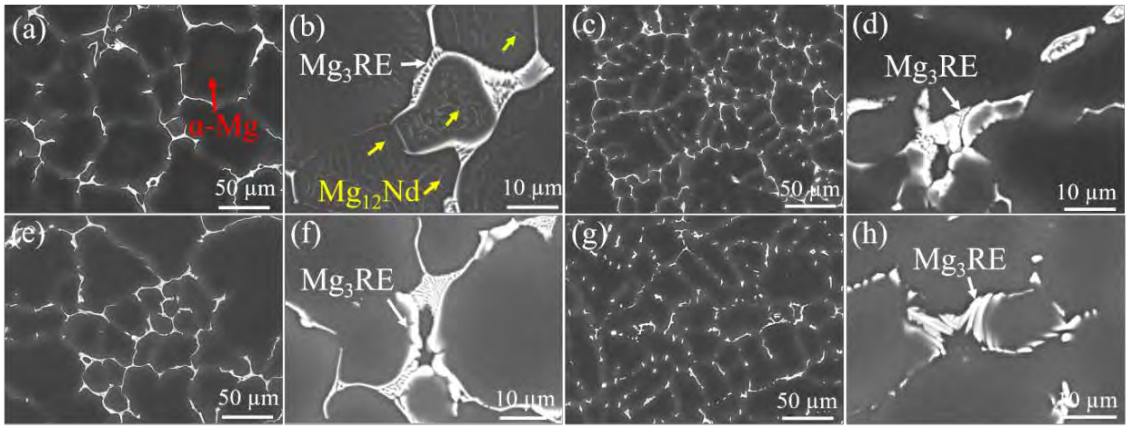

Fig. 6. BSE micrographs of as cast (a) El21 alloy, (c) El21+0.25% Al alloy, (e) El21+0.75% AlN composite and (g) El21+1% AlN/Al composite. Their corresponding magnified microstructures of as cast (b) El21 alloy, (d) El21+0.25% Al alloy, (f) El21+0.75% AlN composites and (h) El21+1% AlN/Al composite.

3.3 Microstructural evolutions

As aforementioned, El21 alloy is mainly composed of Mg, RE (RE indicates Nd and Gd elements), Zn and Zr elements. By adding pure Al, AlN NPs and the mixture of AlN/Al NPs into El21 alloy, the chemical reactions possibly take place among RE, Zr, Al and AlN NPs. Some additional phases might then be formed. In this section, the microstructural evolutions

of Al-Zr and Al-RE phases in El21 and El21 alloys with additives of 0.25%, 0.75% AlN and 1% AlN/Al are discussed based on BSE micrographs.

3.3.1 Al-Zr phase evolution

(1) El21 alloy

Fig. 7(a) shows the BSE micrograph of El21 alloy using HSDT sheared at 3000 rpm for 1 min. Besides the network Mg_3RE eutectic phase, some brighter phases were also observed at the grain boundaries (red arrows). Especially in the magnified area, many irregular particulates were agglomerated. EDS result shows that these particulates have relatively high contents of Zr, Mg and O (Fig. 7(b)), which are assumed as a combination of divorced Zr and MgO particles.

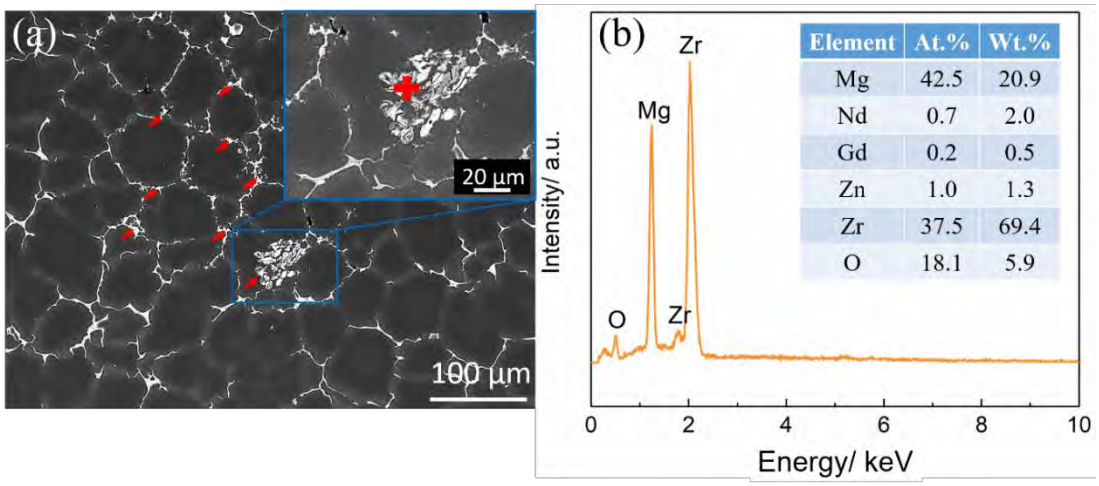

Element	At.%	Wt.%
Mg	42.5	20.9
Nd	0.7	2.0
Gd	0.2	0.5
Zn	1.0	1.3
Zr	37.5	69.4
O	18.1	5.9

Fig. 7. (a) BSE micrograph of El21 alloy and (b) corresponding EDS analysis at the “red cross” position in (a).

(2) El21+0.25% Al alloy

By adding 0.25% Al in El21 alloy, Zr did not retain as independent particulate any more in the matrix because Al is inclined to react with it to form Al-Zr compounds, such as Al_3Zr, Al_2Zr_3 and Al_2Zr [17]. Our previous paper [12] has already reported that two types of Al-Zr particulates, Al_2Zr (orange arrow) and Al_2Zr_3 (blue arrow), were identified in the El21+0.25% Al alloy (Fig. 8). Detailed analyses can be found in [12].

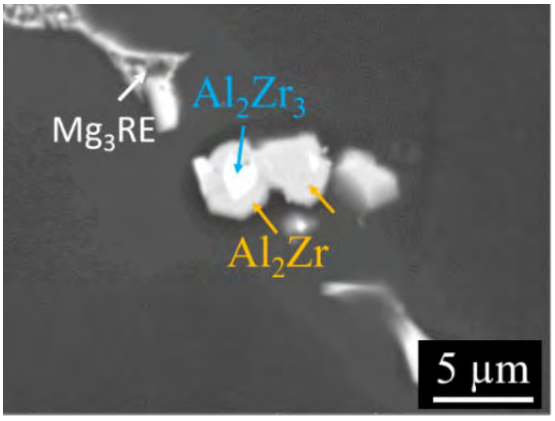

Fig. 8. BSE micrograph of El21+0.25% Al alloy showing the Mg_3RE, Al_2Zr and Al_2Zr_3 phases.

(3) El21+0.75% AlN

Fig. 9(a) shows the BSE micrograph of El21+0.75% AlN with continuous Mg_3RE phase and some fine particulates inside the α-Mg grain (red arrow). Its magnified microstructure reveals that although the morphologies of these fine particulates are similar, their compositions are different (Fig. 9(b)). EDS results indicate that these particulates with orange and blue arrows are mainly made up of Al and Zr (Fig. 9(c) and (d)). Their atomic ratios of Zr to Al were obtained as 0.56 and 1.33, which should correspond to Al_2Zr (Zr/Al = 0.5) and Al_2Zr_3 (Zr/Al = 1.5) phases, respectively. He et al. [18] investigated the formation of reaction layer at the interface between Zr and AlN. They also detected the Al_3Zr and Al_2Zr phases by XRD analysis. It can then be concluded that there should be a chemical reaction between AlN NPs and Zr in El21+0.75% AlN composite. Koltsov et al. [19] verified that Zr can react with AlN according to the following Eq. (1):

$$Zr + AlN \rightarrow ZrN + Al \quad (1)$$

Based on the Gibbs Energies calculations, they claimed that this reaction could be proceeded fully. According to Eq. (1), Al atoms were released during this chemical reaction. It is well reported that many kinds of Al-Zr phases could be formed according to Al-Zr phase diagram, such as Al_2Zr_3, Al_2Zr and Al_3Zr etc. [17, 20]. Therefore, it is assumed that Al_2Zr and Al_2Zr_3 phases can be formed by the following Eq. (2-3):

$$Zr + 2\ Al = Al_2Zr \quad (2)$$

$$3\ Zr + 2\ Al = Al_2Zr_3 \quad (3)$$

These formation procedures are similar to that of Al_2Zr and Al_2Zr_3 particulates reported in El21+0.25% Al alloy [12]. In addition, the reaction products of ZrN and Al in Eq. (1) might not be completely separated. Therefore, the particles marked with green arrows in Fig. 9(b) contains Al, Zr, and N elements, which can be confirmed by corresponding EDS result in Fig. 9(e)).

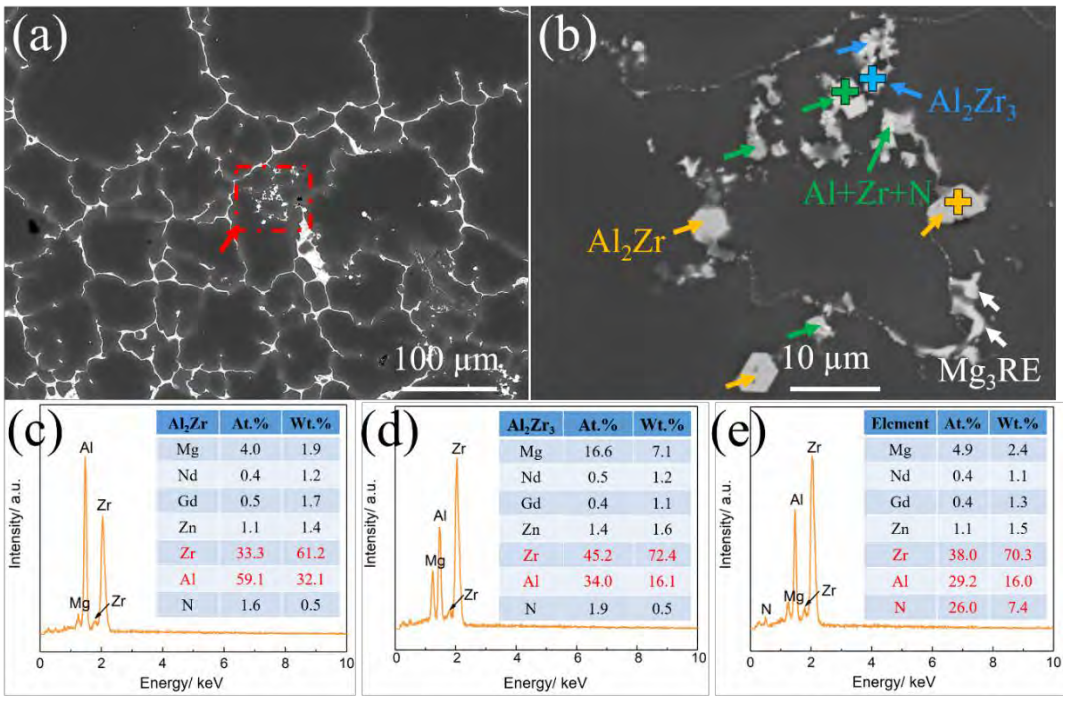

Fig. 9. (a) BSE micrographs of as cast El21+0.75% AlN composite, (b) the magnified image of position in (a) marked with "red arrow", which shows the existence of Al_2Zr, Al_2Zr_3 phase and (Al+Zr+N)-rich particles. The corresponding EDS results of (c) Al_2Zr (position marked with "orange cross" in (b)), (d) Al_2Zr_3 (position marked with "blue cross" in (b)) and (f) (Al+Zr+N)-rich particles (position marked with "green cross" in (b)) were also presented.

It is worth noting that regarding to the chemical reaction Eq. (1), an additional phase ZrN was formed. To further validate the existence of ZrN phase in El21+0.75% AlN, Fig. 10(a) reveals two different areas with light grey (orange arrows) and bright grey (green arrows) colors in El21+0.75% AlN NPs, respectively. The light grey area marked with an "orange cross" has a high content of Zr and N (Fig. 10(b)), which is considered as the ZrN particle. López-Pérez et al. [21] also analyzed the Zr adsorption and incorporation process on AlN (0001) surface. They confirmed the existence of interfacial compound ZrN on the surface of AlN. Koltsov et al. [19] further reported that ZrN phase is actually a compound with a large non-stoichiometric ZrN_{1-y} domain, where *y* change depends on the thermodynamic activity of Zr. The bright grey area

marked with “green cross” has higher contents of RE and Al elements besides Zr and N elements (Fig. 10(c)). Gromov et al. [22] proposed that the formation enthalpies of nitrides for Al and Zr elements are -319 (AlN) and -371 (ZrN) kJ/(mole Me), respectively, indicating that the formation of ZrN is more favorable than that of AlN in terms of thermodynamic properties. Hence, when Zr element exists, AlN NPs are inclined to lose the N atoms for the formation of ZrN phase, and a certain content of Al atoms were then released from AlN NPs. This process is also in good agreement with the Eq. (1). The released Al atoms on the surface of ZrN were more likely to attract the RE element, which is attributed to the low standard molar enthalpy of formation for Al-RE compound [23]. Therefore, a high content of RE and Al was detected in Fig. 10(c). Apart from the observations of ZrN with RE enrichment, the separated ZrN particle was also observed in Fig. 10(d), which was confirmed by EDS analysis with relatively high contents of Zr and N (Fig. 10(e)). According to Eq. (1), Al atoms were released in addition to the formation of ZrN particles. As a result, a higher content of Al at P1 was detected close to the ZrN particle (Fig. 10(f)). The particle at P1 is (Al+Zr+N)-riched, which is similar to that particles found in Fig. 9(b) marked with green arrows.

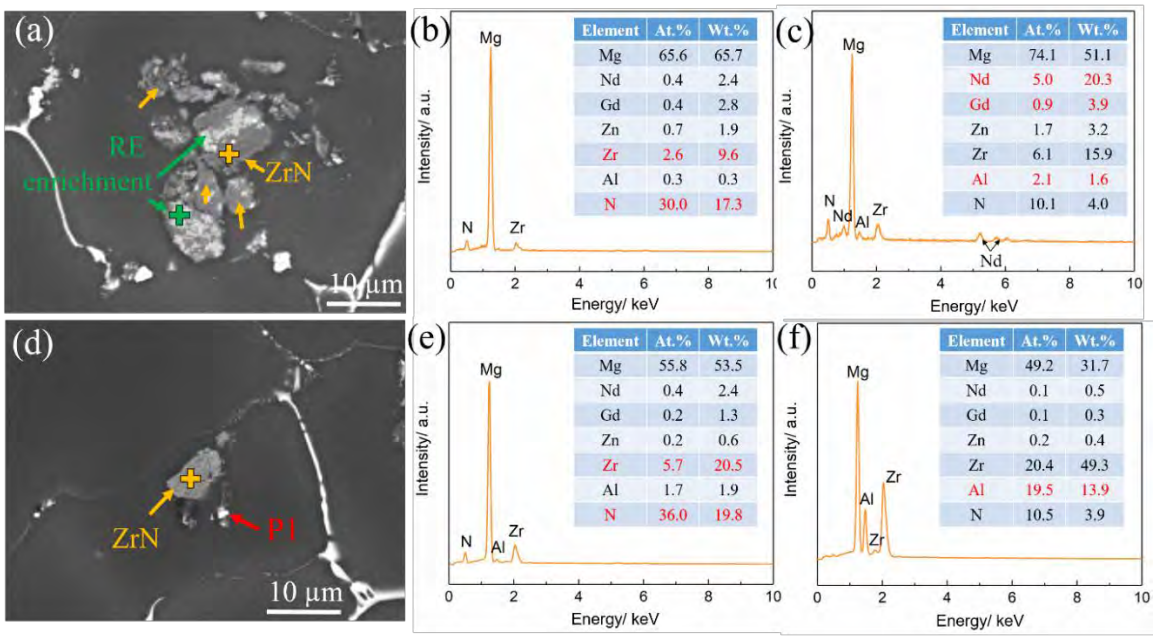

Fig. 10. (a) BSE micrograph of as cast El21+0.75% AlN composite, (b) EDS result of ZrN at the position marked with “orange cross” in (a), (c) EDS result of RE enrichment at the position marked with “green cross” in (a) and (d) the separate ZrN clusters. EDS results of (e) ZrN at the position marked with “orange cross” in (d) and (f) (Al+Zr+N)-rich particle at P1 in (d).

(4) El21+1% AlN/Al composite

By adding 1% AlN/Al NPs in El21 alloy using HSDT at 720 °C, AlN NPs could not be dissolved in the matrix due to its high melting point (2197 ° [24]) while Al NPs were easily dissolved into the matrix because of their lower melting point (660 °C [25]). The AlN NPs were possibly agglomerated as clusters due to their relatively poor wettability. In Fig. 11(a), some visible clusters are agglomerated in the matrix (orange arrows). The area marked with red dashes in Fig. 11(a) was magnified in Fig. 11(b). The bright cluster consists of abundant extremely fine particles. According to the EDS mapping results of Fig. 11(b) (Fig. 11(c-i)), it is found that even the morphology of these particles are similar, there still exists a compositional difference inside the cluster. Fig. 11(d-e) reveal a high content of Al and N in the cluster (red arrows). Its corresponding EDS point result in Fig. 11(j) shows that it contains 53.3 at.% Al and 19.2 at.% N, indicating the existence of AlN NPs in the cluster. Interestingly, it should be noticed that Zr element was mainly found at the outer layer of cluster (white arrows in Fig. 11(f)). It demonstrates that Zr atoms were segregated at the outer surface of AlN NPs and reacted with them.

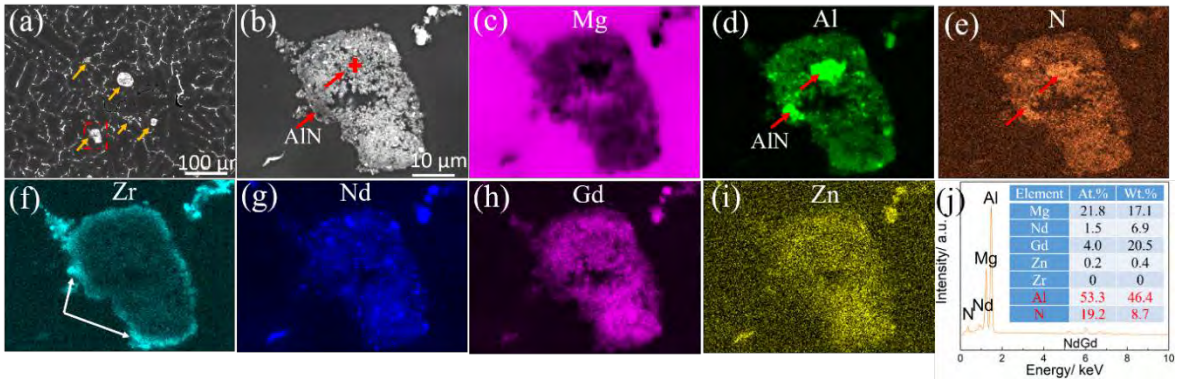

Fig. 11. (a) BSE micrograph of El21+1% AlN/Al composite, (b) magnified image in (a) with "red dashes", (c-i) EDS mapping of (b) showing the results of Mg, Al, N, Zr, Nd, Gd and Zn element, respectively. (j) EDS point result at the "red cross" position in (b).

The separate ZrN particles were also detected in El21+1% AlN/Al composite (Fig. 12(a) and (c)), which originated from the reaction product in Eq. (1). But another reaction product Al was measured to be little. However, the Zr atoms did not consume all the AlN NPs completely. AlN-rich particles were still observed in the El21+1% AlN/Al (Fig. 12(b)). At these particles, little Zr with relatively high amount of RE was measured. This RE enrichment was also observed in El21+0.75% AlN (Fig. 10(a)), implying that AlN NPs are inclined to attract RE atoms during solidification. Unlike the previous mentioned alloys, in El21+1% AlN/Al

composites, the blocky Al-Zr phase was not detected. This suggests that the formation of Al-Zr particles was suppressed. In contrast, Al_2Zr_3 or Al_2Zr phases can be easily observed in El21+0.25% Al alloy and El21+0.75% AlN composite (Fig. 8 and Fig. 9(b)).

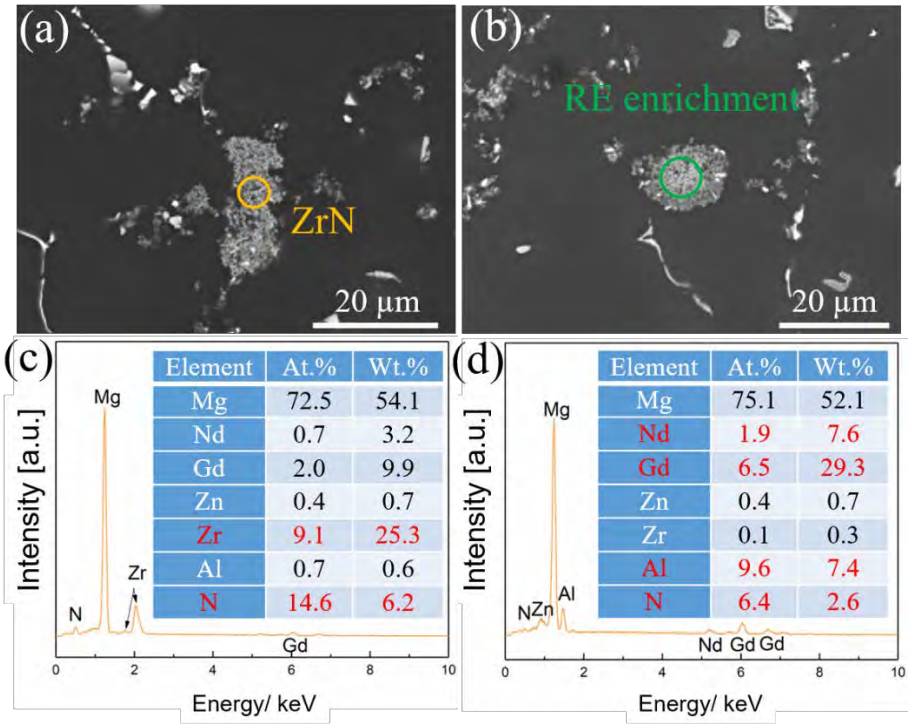

Fig. 12. BSE micrographs of El21+1% AlN/Al showing (a) ZrN particles (b) RE enrichment on the AlN particles and their corresponding EDS results (c) and (d), respectively.

3.3.2 Al-RE phase evolution

It is well known that Al can react with REs to form Al-RE phases, such as $Al_{11}RE_3$ and Al_2RE [26]. A small particulate, which was already verified as Al_2RE phase [12], was observed close to Mg_3RE phase in El21+0.25% Al alloy (Fig. 13(a-c)). Similarly, Al_2RE phase with granular shape was also detected adjacent to Mg_3RE phase in El21+0.75% AlN (Fig. 13(d-f)). These Al_2RE particles have a very slight quantity in both El21+0.25% Al and El21+0.75% AlN. They only exist in some certain regions and are unable to be detected by XRD. However, in El21+1% AlN/Al, the amount of Al_2RE phases is larger (Fig. 13(g-i)). Its content is high enough to be detected by XRD (Fig. 4(d)). Fig. 13(h) shows that the Al_2RE phase (orange arrows) is interconnected with Mg_3RE phase (white arrows), demonstrating that the Al_2RE phase (orange arrows) is also another dominant eutectic phase in El21+1% AlN/Al composite. These Al atoms in Al_2RE phase, either from Al addition or AlN NPs addition, could react with RE to

form a large amount of Al_2RE phase. In contrast, in El21+0.25% Al alloy and El21+0.75% AlN composite, a much lower quantity of Al atoms is available to react with RE atoms.

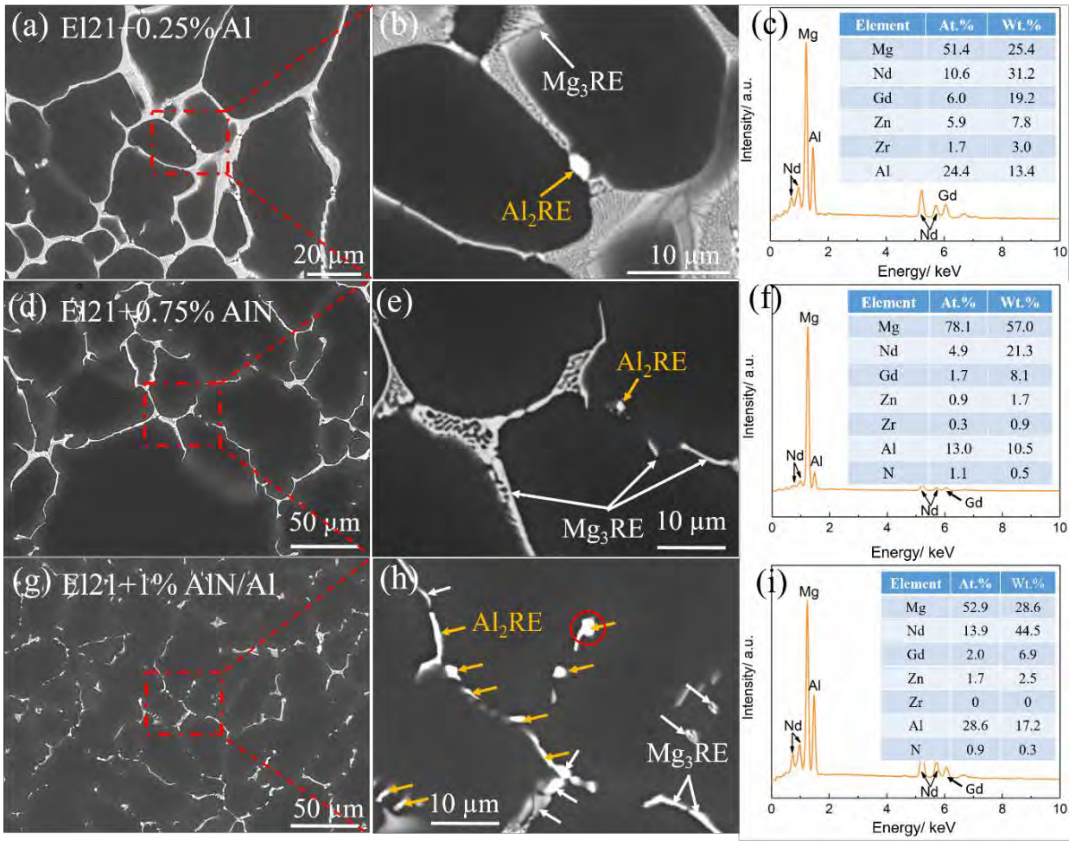

Fig. 13. BSE micrographs at lower and higher magnifications for the as cast (a-b) El21+0.25% Al alloy, (d-e) El21+0.75% AlN composite and (g-h) El21+1% AlN/Al composite, respectively. Their corresponding EDS results of Al_2RE phase in (c) El21+0.25% Al alloy (at the position marked with "orange arrow" in (b)), (f) El21+0.75% AlN composite (at the position marked with "orange arrow" in (e)) and (i) El21+1% AlN/Al composite (at position marked with "red circle" in (h)) were also presented.

3.4 Microstructures after creep deformation

To compare the microstructures after creep for these four materials, El21+0.25% Al alloy, El21+0.75% AlN composite and El21+1% AlN/Al NPs composite were crept under the same condition (140 MPa at 240 °C for the creep time 266 h), at which they all reached to the secondary creep region. But for El21 alloy with the worst creep resistance (Fig. 1(d)), under such condition it could not endure for the whole creep process. Its creep time was then defined as that when its secondary creep region was achieved under 140 MPa at 240 °C. Fig. 14(a-h) shows the representative orientation imaging microscopy (OIM) and their corresponding kernel

average misorientation (KAM) maps for El21 alloy, El21+0.25% Al alloy, El21+0.75% AlN composite and El21+1% AlN/Al composite. The results of OIM (Fig. 14(a-d)) show that no apparent difference in the grain orientation is found among these alloys. Nevertheless, their KAM maps indicate their different levels of stress concentrations (Fig. 14(e-h)). The red regions in KAM maps have a higher stress concentration and green areas indicate a relatively lower stress concentration after creep deformation (as illustrated by the legend in Fig. 14(e-h)). In the crept El21 alloy, obvious local stress concentrations were characterized, especially along grain boundaries. Its average number fraction for KAM is 3.26. With the addition of 0.25% Al in El21 alloy, no obvious change in the average number fraction of KAM is observed (Fig. 14(f)). By adding 0.75% AlN into El21 alloy, the local stress concentrations are alleviated with a relatively lower average number fraction of 3.02 (Fig. 14 (g)). With the addition of 1% AlN/Al NPs in El21 alloy, the green area fraction obviously increases and the average number fraction of KAM decreases to 2.81 (Fig. 14(h)). The local stress concentrations are apparently alleviated in the crept El21 alloy with the addition of 1% AlN/Al NPs. The distributions of misorientation angle reveal that all these four alloys have a quite high fraction of low-angle boundaries (LABs) between 0-5° after creep deformation (Fig. 14(i-l)).

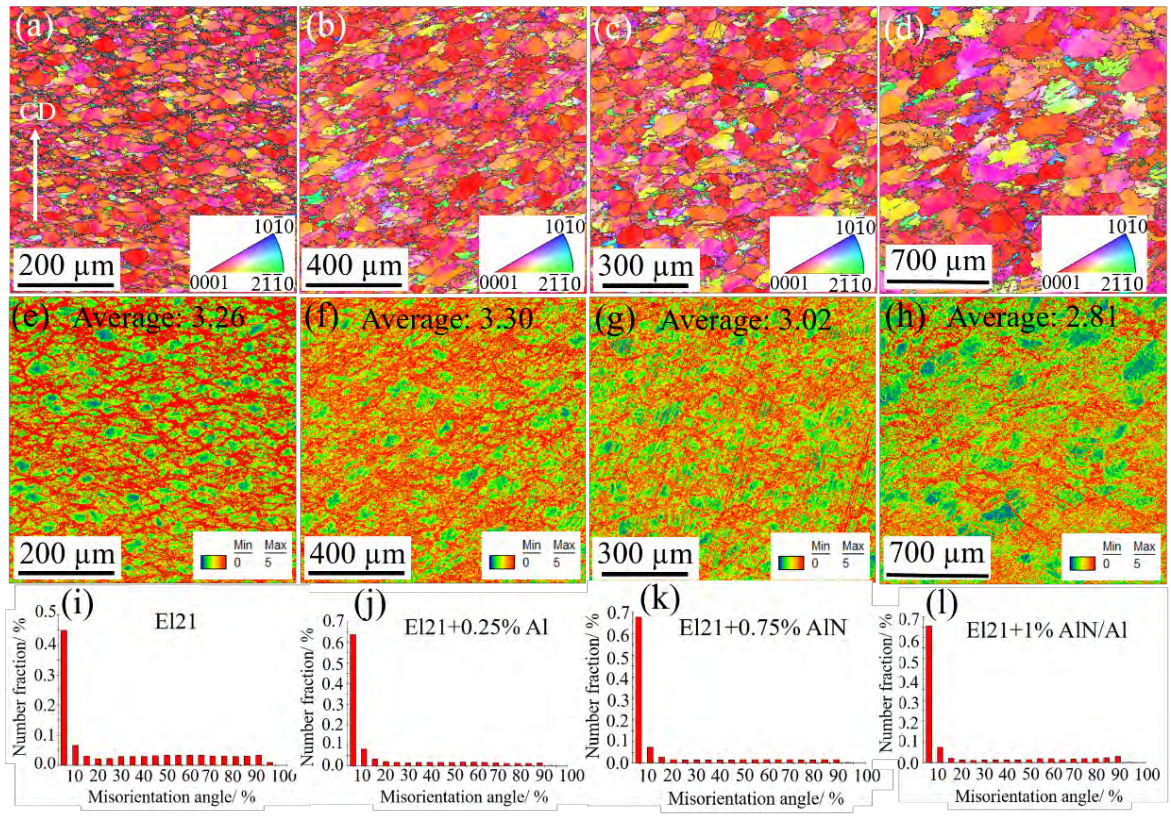

Fig. 14. Orientation imaging microscopy (OIM) of crept (a) El21 alloy, (b) El21+0.25% Al alloy, (c) El21+0.75% AlN composite and (d) El21+1% AlN/Al composite. Kernel average misorientation (KAM) maps of crept (e) El21 alloy, (b) El21+0.25% Al alloy, (c) El21+0.75% AlN composite and (d) El21+1% AlN/Al composite under 140 MPa at 240 °C. The perpendicular direction showing the crept direction (CD) in (a). The misorientation angle distributions of (i) El21, (j) El21+0.25% Al, (k) El21+0.75% AlN and (l) El21+1% AlN/Al after creep are given.

4. Discussion

4.1 Creep mechanism

The power-law equation Eq. (4) describes the dependence of minimum creep rate $\dot{\varepsilon}_s$ on the applied stress σ and temperature T (in Kelvin) [27-29]:

$$\dot{\varepsilon}_s = A\sigma^n \, exp\left(-\frac{Q_c}{RT}\right) \tag{4}$$

Where A is a material related constant, Q_c is the activation energy, R is the gas constant, T is the absolute temperature and n is the stress exponent that gives information about the deformation mechanism taking place during creep. n values can be calculated by the slope of double logarithmic plotting of $\dot{\varepsilon}_s$ against σ. They were inserted in the plots (Fig. 15(a)), which are around 5 for all these four alloys. However, as for the more complex materials with particle or precipitate strengthening, their obtained stress exponents are usually quite high compared with theoretical values [29, 30]. Zhang [31] reported that the stress exponents of die-cast Mg-Al alloy AS21 were very high with values in a range of 13-19. It is impossible to interpret its creep mechanism directly only based on the n values. Li and Langdon [32] introduced a concept of threshold stress σ_{thr} to indicate the stress where no creep deformation occurs. This is related to the dispersoid-strengthening in metallic material, in which the dispersoid obstacles can impede the movement of the dislocations [30]. In [32], they developed a simple model to estimate the threshold stresses. A strain rate of 10^{-10} s^{-1} was considered to be the lowest strain rate corresponding to a creep strain with only ~1% in laboratory experiments for testing 3 years. Extrapolating the double logarithmic plots of Fig. 15 (a) to a strain rate of 10^{-10} s^{-1} gives the threshold stress value (Table 3). The σ_{thr} of El21+0.25% Al alloy and El21+0.75% AlN composite are 28.7 and 24.6 MPa, respectively, which are distinctly higher than that of unreinforced-El21 alloy (16.7 MPa). Among these four materials, El21+1% AlN/Al composite

has the highest σ_{thr} with a value of 35.3 MPa, demonstrating that the addition of 1% AlN/Al NPs in El21 alloy has the strongest strengthening effect to enhance the interactions between particles and dislocations.

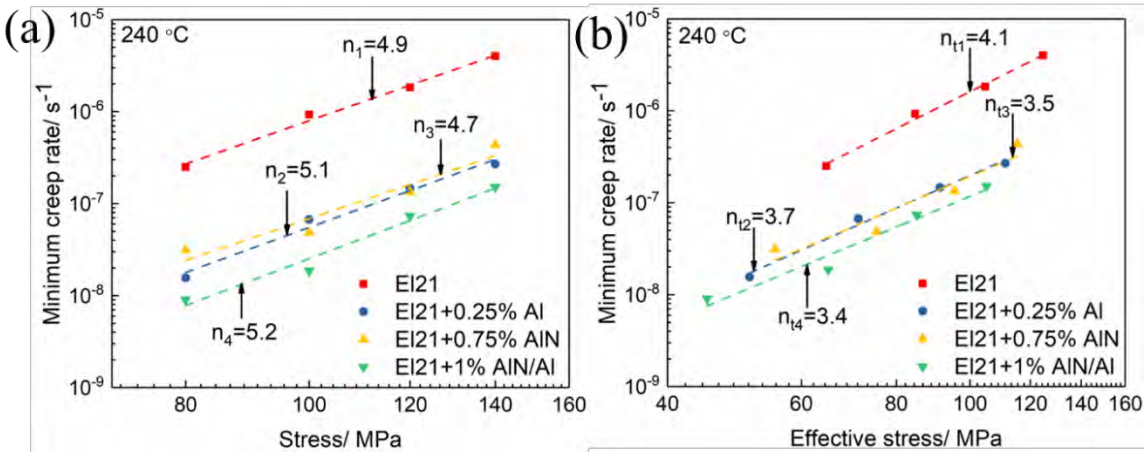

Fig. 15. Double logarithmic plots of (a) the stress dependence of minimum creep rate and (b) the effective stress dependence of minimum creep rate for El21 alloy, El21+0.25% Al alloy, El21+0.75% AlN composite and El21+1% AlN/Al composite at 240 °C.

Table 3. Values of stress exponent n, true stress exponent n_t and threshold stress σ_{thr}.

No.	Materials	n	n_t	σ_{thr}/ MPa
1	El21	4.9	4.1	16.7
2	El21+0.25% Al	5.1	3.7	28.7
3	El21+0.75% AlN	4.7	3.5	24.6
4	El21+1% AlN/Al	5.2	3.4	35.3

Based on the introduction of threshold stress σ_{thr} (Eq. (5)), Eq. (4) is then modified to Eq. (6) as below:

$$\sigma_{eff} = \sigma - \sigma_{thr} \tag{5}$$

$$\dot{\varepsilon}_s = A(\sigma_{eff})^{n_t} \exp\left(-\frac{Q_C}{RT}\right) \tag{6}$$

n_t is the true stress exponent, which is determined by the slope of double logarithmic plots of effective stress σ_{eff} against $\dot{\varepsilon}_s$ (Fig. 15(b)). The n_t values of these four materials are around 3-4, which are lower than n values (Fig. 15(a)). It is well documented that stress exponent n=1 is related to the diffusion deformation mechanism, n=3 is connected to the viscous glide of dislocation, n=5 corresponds to the dislocation climbing at elevated temperature and n=7 to the

dislocation climbing at low temperatures [33-35]. It is therefore concluded that the dominant deformation mechanism during creep at 240 °C for these four materials is viscous glide of dislocation. In fact, this conclusion is in good agreement with the characterizations of LABs in Fig. 14(i-l). S. Gourdet et al. [36] proposed that the LABs were usually accumulated progressively by the dislocations during strain hardening. Dislocation glide preferred to reinforce the generations of LABs. Shi et al. [37] also observed the LABs in the crept Mg-4Y alloy and concluded that the active dislocation is mainly basal slip during deformation.

4.2 Individual/synergistic effects of Al and AlN NPs on microstructural evolutions

4.2.1 Individual effects of Al and AlN

The phase evolutions with additions of 0.25% Al, 0.75% AlN and 1% AlN/Al in El21 alloy are schematically illustrated in Fig. 16. For the unmodified El21 alloy, it is mainly made up of network eutectic Mg_3RE, tiny needle-like $Mg_{12}Nd$ phases and isolated Zr particles (Fig. 16(a)). It is worth noting that many MgO particles were also formed close to Zr particles (Fig. 7). Fan et al. [38] discussed the influence of HSDT on the solidification process of AZ91D alloy. They found that many fine MgO particles were formed in Mg matrix after high shearing. HSDT could result in the formation of MgO particles in the matrix due to the gas sucking caused by high shearing during melting.

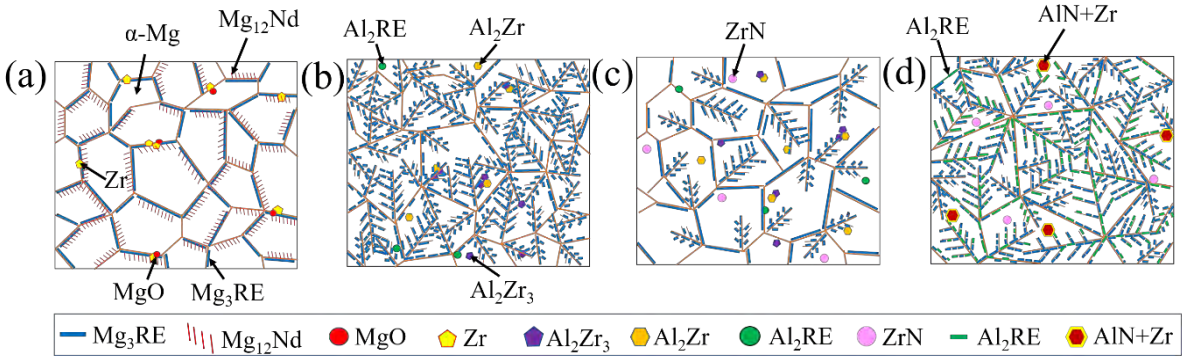

Fig. 16. Schematic illustrations of the microstructural evolutions for (a) El21 alloy, (b) El21+0.25% Al alloy, (c) El21+0.75% AlN composites and (d) El21+1% AlN/Al composite.

By adding 0.25% Al in the El21 alloy, the morphology of intermetallic particles was changed from typical network to pronounced dendrites. The distribution of Mg_3RE phases also became more dispersive than that in the unmodified El21 alloy. Lath-like $Mg_{12}RE$ precipitates near the

eutectic phases were disappeared in El21+0.25% Al alloy. It was reported that the formation of $Mg_{12}Nd$ precipitates is due to the supersaturation of Nd in the matrix [39, 40]. Our previous work [12] proposed that the disappearance of $Mg_{12}Nd$ precipitates in El21+0.25% Al alloy was attributed to the formation of Al_2RE phase, which consumed many RE atoms and alleviated the supersaturation of Nd in α-Mg matrix. Interestingly, in this alloy, Zr particles disappeared and some Al_2Zr/Al_2Zr_3 phases occurred instead. It is known that Zr acts as grain refiner in the Al-free Mg-based alloys [41]. When it was bound in Al_2Zr/Al_2Zr_3 phases, it did not work as grain refiner any longer, thus leading to the grain coarsening in El21+0.25% Al alloy. In addition to these Al-Zr phases, some dissociative Al_2RE particles were also formed by the reaction of Al with RE atoms.

With the separate addition of 0.75% AlN NPs in El21 alloy, similar grain coarsening and dendritic morphology of the intermetallic particles were also observed. In this study, besides these same Al_2Zr, Al_2Zr_3 and Al_2RE phases observed in El21+0.25% Al alloy, some additional ZrN particles were formed due to the chemical reaction of AlN NPs with Zr in Eq. (1) in El21+0.75% AlN composites (Fig. 16(c)). With such a chemical reaction, around or at ZrN particles a discernible amount of Al atoms was released. Consequently, they attracted more RE atoms on the surface of ZrN particles.

4.2.2 Synergistic effects of Al and AlN

When the mixture of 0.25% Al and 0.75% AlN NPs was added to the El21 alloy, the grain size was further increased from 59.4±1.6 μm for El21 alloy to 463.5±17.5 μm for El21+1% AlN/Al composite. This is attributed to the consumption of Zr by the reaction with AlN NPs in Eq. 1, which results in a loss of grain refiner and leads to the grain coarsening. Moreover, in this composite, the morphological modification of the intermetallic particles was further enhanced with many finer and more homogeneous particles in the α-Mg matrix (Fig. 16(d)). These phases are mainly composed of intermetallic Mg_3RE and Al_2RE phases. Noting that the Al_2RE phase shows a much larger amount in El21+1% AlN/Al than that in El21+0.25% Al and El21+0.75% AlN (green line in Fig. 16(d)). In contrast, in this composite, it is difficult to observe any blocky Al_2Zr/Al_2Zr_3 phases. A certain content of Zr was detected at the outer layer of the AlN particles in El21+1% AlN/Al composites (Fig. 11(f)). In addition, some ZrN particles were formed in El21+1% AlN/Al as that found in El21+0.75% AlN. Previous research [42] selected the metal elements Al and Zr to study their strength of interfacial adhesion to AlN based on the nucleation thermodynamics. The adhesion strength described how easy the film may grow on the AlN

substrate and develop the interface. It was proposed that Zr has a smaller negative driving force on the AlN substrate than Al, corresponding to a larger tendency of nucleation on AlN than Al element if under the same condition. This phenomenon well supports that in El21+1% AlN/Al, Zr preferentially nucleated at the outer layer of the AlN particles instead of Al. In this paper [42], it was also reported that the interfacial adhesion between Al and AlN is relative weak due to their lattice mismatch. Owing to the preferential reaction of Zr with AlN and the weak adhesion of Al and AlN, the 0.25% Al from the mixture of 1% AlN /Al NPs was rejected by AlN and Zr during solidification. Al atoms then have more chances to react with RE to form more amount of stable Al_2RE phase. As indicates by Eq. (1), a certain amount of Al atoms was also released when AlN NPs reacted with Zr. This also leads to the formation of more amount of Al_2RE phases in El21+1% AlN/Al composite. Since Zr tended to nucleate on the surface of AlN NPs instead of Al and Al atoms were largely consumed by RE, the chemical reaction of Al with Zr was suppressed. This explanation is also consistent with the observations in El21+1% AlN/Al composite, in which no blocky Al-Zr phases could be found.

Based the above discussion, the formation processes of phases in El21+0.25% Al alloy, El21+0.75% AlN and El21+1% AlN/Al composite are summarized in Table 4. The effects of individual Al and AlN additions on the microstructural evolutions can be summarized as following:

(1) The individual addition of pure Al or AlN can lead to the formation of Al_2Zr_3, Al_2Zr and Al_2RE phases in El21 alloy.

(2) Their additions can change the intermetallic morphology from network to pronounced dendrite. Especially, Al addition is more efficient to modify the intermetallic morphology than AlN addition.

(3) An additional phase ZrN was formed in El21 alloy with the addition of 0.75% AlN.

The synergistic effects of Al and AlN combinative addition are illustrated as following:

(1) The intermetallic morphology was further modified with denser and more homogeneous distribution than that by individual additions of Al or AlN.

(2) Much more amount of Al_2RE phase was formed in El21+1%AlN/Al composite. The Al atoms in Al_2RE phase were from both Al and AlN NPs.

(3) The formation of blocky Al_2Zr_3 and Al_2Zr phases was suppressed. Instead, Zr nucleated at the outer layer of AlN clusters and reacted with them more preferentially.

Table 4. Phase formation processes in El21+0.25% Al, El21+0.75% AlN and El21+1% AlN/Al alloy.

No.	Materials	Formation process
1	El21+0.25% Al	Al → Zr = Al_2Zr + Al_2Zr_3; Al → RE = Al_2RE
2	El21+0.75% AlN	AlN ⟷ Zr = ZrN + Al; Zr → = Al_2Zr+Al_2Zr_3; RE → = Al_2RE
3	El21+1% AlN/Al	Zr → AlN = ZrN + Al; Zr → Al; Al → RE = Al_2RE

4.3 Individual/synergistic effects of Al and AlN on the creep resistance

4.3.1 Individual effects of Al and AlN

As discussed in the section of 3.1, El21 alloy has the worst creep resistance among these four alloys. With the additions of 0.25% Al or 0.75% AlN in El21 alloy, their creep resistance is quite close, but obviously better than that of unreinforced El21 alloy. This is mainly ascribed to the higher fraction of intermetallic particles in El21+0.25% Al alloy and El21+0.75% AlN composite (Fig. 5). These intermetallic particles could effectively hinder the dislocation motions and grain boundary sliding during creep, and thus giving a rise in the creep properties.

With adding low content of Al (0.25%) in El21 alloy it achieves a comparable strengthening effect in creep resistance to that in El21+0.75% AlN composite (Table 2). It can then be concluded that, at the same contents of Al and AlN, the strengthening effect from Al on the creep resistance should be much higher than that from AlN NPs. As depicted in Fig. 5, both the additions of 0.25% Al and 0.75% AlN NPs in El21 alloy influence the morphological modification of intermetallic particles. However, the dendritic morphologies of intermetallic particles in El21+0.25% Al alloy is slightly obvious than that in El21+0.75% AlN composite. Jiang et al [43] reported that with the addition of Al element the typical dendritic growth was observed in Mg-5Sn-0.3Li alloy due to the constitutional supercooling ahead of solid/liquid interface. Our previous paper [14] claimed that the existence of AlN NPs could reduce the effective solute diffusivity ahead of the solid/liquid interface and thus also cause branching

dendrites. Unlike AlN particles existing in solid state, Al dissolved into the melt during melting. Thus, their influence on the dendritic growth, intermetallic morphology and distribution should be different. As for the solid AlN, it may influence the dendritic growth and intermetallic distribution via their disturbing the solute diffusion and dendritic growth. But for Al, it could segregate in the front of solid/liquid interface, resulting a constitutional supercooling ahead of the solid/liquid interface. Such a constitutional supercooling definitely affected the subsequent growth of dendrites as reported by Jiang [43]. Based on the present results, Al is more effective to modify the morphology and distribution of intermetallic particles than AlN, indicating that the generated supercooling ahead of the solid/liquid interface play a more important role in influencing the dendritic growth than the external disturbance from the solid AlN particles. On the other hand, 0.25% Al could react with Zr and RE atoms to form Al-Zr and Al-RE phases directly. While in El21+0.75% AlN the Al atoms was released from AlN NPs by the chemical reaction of AlN with Zr (Eq. (1)). The utilization efficiency of Al atoms to combine with RE depends on whether the chemical reaction was complete. In addition, the former alloy Al existed in the element state, but in the latter it is in compound. It can then be expected that Al-Zr and Al-RE phases are easier to be formed in El21+0.25% Al alloy than that in El21+0.75% AlN. Kabirian et al. [44] investigated the effect of Zr content on the creep resistance of AZ91 alloy. They found that the creep resistance of AZ91 alloy was increased due to the favorable formations of Al_3Zr_2 and Al_2Zr intermetallic compounds. Zhu et al. [45] also reported Al_2RE phase has a good thermal stability without any decomposition at elevated temperature, which favors the creep resistance of AE44 alloy. Consequently, with the same percent additions of Al and AlN NPs, Al addition is more effective in enhancing the creep resistance of El21 alloy than AlN NPs.

4.3.2 Synergistic effects of Al and AlN

With mixed additions of 0.25% Al and 0.75% AlN (1% AlN/Al) in El21 alloy, its intermetallic particles are much thinner and their distribution is more homogeneous. Such microstructure could be more effective to inhibit the dislocation movement and grain boundaries and thus improve the creep properties. It is noteworthy that the fraction of intermetallic particles in El21+1% AlN/Al composite (10.4%) is slightly lower than that in El21+0.25% Al (12.0%) (Fig. 5(b) and (d)), but its creep resistance is much better than that in the latter. Firstly, the dominant intermetallic particles are different in the matrix of these two alloys. In El21+0.25% Al alloy Mg_3RE is the main intermetallic particle, while Mg_3RE and Al_2RE particles are the

two dominant phases in El21+1% AlN/Al composite. It was reported that Al_2RE has a higher melting point (1200 °C) than Mg_3RE phase 780 °C [46], indicating a higher thermal stability of Al_2RE than that of Mg_3RE phase. Previous papers [47, 48] also reported that Al_2Nd has a much higher elastic modulus 121.44 GPa than that of Mg_3RE 65.83 GPa. It can provide a higher strength to hinder the dislocation motions and transfer the applied load to the matrix more effectively during creep. Secondary, the distribution of intermetallic particles in El21+0.25% Al alloy is not as homogeneous as that in El21+1% AlN/Al composite (Fig. 5(b)). Such microstructure is less effective to hinder the dislocation movement and to alleviate the stress concentration. This can further be supported by the results of KAM maps (Fig. 14). El21+1% AlN/Al composite has the lowest local stress concentrations among these four alloys.

In order to evaluate the load transfer efficiency of these intermetallic particles in El21+0.25%Al alloy, El21+0.75% AlN composite and El21+1%AlN/Al composite quantitatively, a load transfer factor α was introduced based on a simplified empirical method [49]. The values of load transfer factor α vary in a range of 0-1, where α=0 indicates no load transfer from particles to the matrix and α=1 indexes that all the applied loads are sustained by the particles. Tian et al. [49] proposed the empirical formula as follows:

$$\frac{\dot{\varepsilon_c}}{\dot{\varepsilon_b}} = (1-\alpha)^{n_t} \tag{7}$$

Where $\dot{\varepsilon_c}$ is the minimum creep rate of the alloy with reinforcement, $\dot{\varepsilon_b}$ is the minimum creep rate of the matrix. In the present work, El21 alloy was considered as the matrix, El21+0.25%Al, El21+0.75% AlN and El21+1%AlN/Al were regarded as the matrix with various reinforcements. When creep begins, the creep temperature and applied stresses are two major factors to influence the creep behaviors. The values of load transfer factor α for El21+0.25%Al, El21+0.75% AlN and El21+1%AlN/Al crept at 240 °C were plotted with respect to the different applied stresses in Fig. 17. It clearly shows that El21+1%AlN/Al composite has a higher load transfer factor ($\alpha > 0.60$) than that of El21+0.25% Al alloy and El21+0.75% AlN composite ($\alpha < 0.60$) (Table 5). This calculation result quantitatively reveals that the intermetallic particles in El21+1%AlN/Al composite are more effective to transfer the loads from the matrix to the particles and to relieve the local stress concentrations during creep deformation. This result is also consistent with the characterizations by KAM maps (Fig. 14).

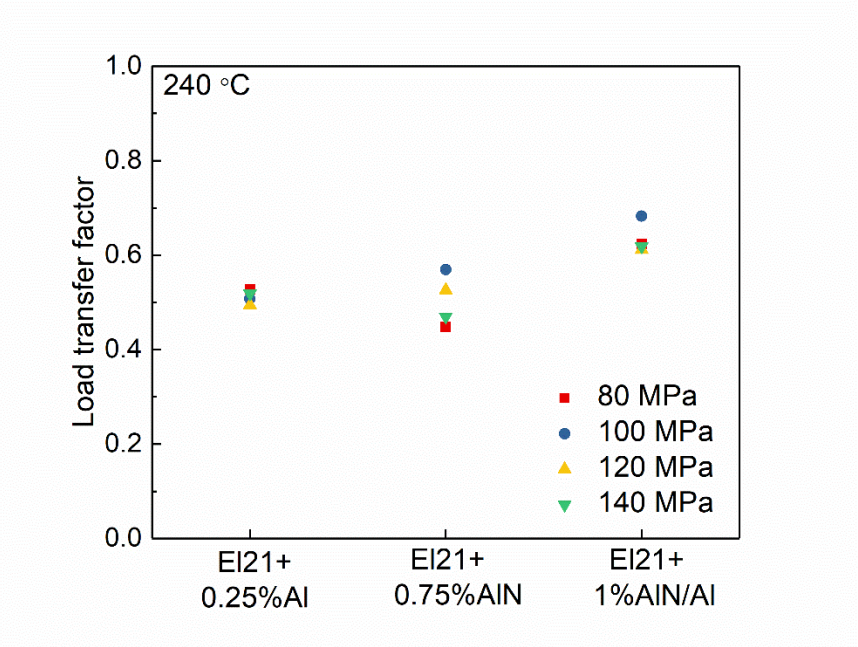

Fig. 17. Comparisons of load transfer factor α for El21+0.25% Al alloy, El21+0.75% AlN composite and El21+1% AlN/Al composite crept under the applied stresses 80-140 MPa at 240 °C.

Table 5. Load transfer factor α of El21+0.25% Al alloy, El21+0.75% AlN composite and El21+1% AlN/Al composite crept at the applied stresses 80-140 MPa at 240 °C.

Stress/ MPa	Load transfer factor α		
	El21+0.25% Al	El21+0.75% AlN	El21+1% AlN/Al
80	0.53	0.45	0.62
100	0.51	0.57	0.68
120	0.49	0.53	0.61
140	0.52	0.47	0.62

5. Conclusions

El21 alloy, El21+0.25% Al alloy, El21+0.75% AlN composite and El21+1% AlN/Al composite were successfully fabricated using HSDT. The individual/synergistic effects of Al and AlN additions on the microstructural evolution and creep resistance of El21 alloy were investigated. The following conclusions are obtained:

(1) The additions of Al, AlN and AlN/Al contribute to the improvement of creep resistance for El21 alloy. The addition of 1% AlN/Al shows the most effective strengthening effect on creep properties of El21 alloy over the stress range from 80 to 140 MPa at

240 °C. With the same weight percent additions of Al and AlN NPs, Al addition is more effective in enhancing the creep resistance of El21 alloy than AlN NPs.

(2) By adding 0.25% Al in El21 alloy, the isolated Zr particles disappears, the blocky Al_2Zr/Al_2Zr_3 and Al_2RE particulates are formed instead. By adding 0.75% AlN NPs, additional ZrN particles are formed due to the chemical reaction of AlN NPs with Zr. By adding 1% AlN/Al NPs, the formation of blocky Al_2Zr/ Al_2Zr_3 is suppressed. A larger amount of Al_2RE phases is formed. This is attributed to the preferential reaction of AlN with Zr, which restricts the formation of Al-Zr phase and subsequently promotes the formation of Al-RE phase.

(3) The dominant deformation mechanism during creep at 240 °C is viscous glide of dislocation for these four alloys. The mixed addition of Al and AlN NPs leads to more homogeneous distribution of intermetallic particles and produces more amount of Al_2RE phase. Such microstructure is more effective to hinder the dislocation movement and grain boundary sliding, transfer the load from matrix and alleviate the stress concentration. Consequently, El21+1% AlN/Al composite exhibits the best creep resistance among all four alloys.

Acknowledges

The authors acknowledge Mr. G. Meister and Mr. Yiming Jin for preparing the alloys and Ms. Petra Fischer for the characterizations of EBSD measurements. Hong Yang gratefully thanks the China Scholarship Council (201606050110) for the award of a fellowship and funding.

References

[1] A. Kiełbus, Microstructure and mechanical properties of Elektron 21 alloy after heat treatment, Journal of Achievements in Materials and Manufacturing Engineering 20(1-2) (2007) 127-130.

[2] B. Mouls, L. Arurault, P.-L. Taberna, C. Bonningue, Macroscopic, thermodynamic, kinetic and microscopic study of nitric acid pickling of Elektron 21 (EV31A) magnesium alloy, Journal of Magnesium and Alloys 2(4) (2014) 363-376.

[3] P. Lyon, I. Syed, S. Heaney, Elektron 21 – An Aerospace Magnesium Alloy for Sand Cast and Investment Cast Applications, Advanced Engineering Materials 9(9) (2007) 793-798.

[4] A. Kielbus, T. Rzychon, R. Przeliorz, DSC and Microstructural Investigations of the Elektron 21 Magnesium Alloy, Materials Science Forum 638-642 (2010) 1447-1452.

[5] S.M. Zhu, M.A. Gibson, M.A. Easton, J.F. Nie, The relationship between microstructure and creep resistance in die-cast magnesium–rare earth alloys, Scripta Materialia 63(7) (2010) 698-703.

[6] B. Smola, I. Stulíková, J. Pelcová, B.L. Mordike, Significance of stable and metastable phases in high temperature creep resistant magnesium–rare earth base alloys, Journal of Alloys and Compounds 378(1) (2004) 196-201.

[7] L. Katsarou, M. Mounib, W. Lefebvre, S. Vorozhtsov, M. Pavese, C. Badini, J.M. Molina-Aldareguia, C.C. Jimenez, M.T. Pérez Prado, H. Dieringa, Microstructure, mechanical properties and creep of magnesium alloy Elektron21 reinforced with AlN nanoparticles by ultrasound-assisted stirring, Materials Science and Engineering: A 659 (2016) 84-92.
[8] R. Daudin, S. Terzi, C. Mallmann, R.S. Martín, P. Lhuissier, E. Boller, A. Pacureanu, L. Katsarou, H. Dieringa, L. Salvo, Indirect improvement of high temperature mechanical properties of a Mg-based alloy Elektron21 by addition of AlN nanoparticles, Materials Science and Engineering: A 688 (2017) 76-82.
[9] A. Saboori, E. Padovano, M. Pavese, C. Badini, Novel Magnesium Elektron21-AlN Nanocomposites Produced by Ultrasound-Assisted Casting; Microstructure, Thermal and Electrical Conductivity, Materials (Basel) 11(1) (2017).
[10] A. Saboori, E. Padovano, M. Pavese, H. Dieringa, C. Badini, Effect of Solution Treatment on Precipitation Behaviors, Age Hardening Response and Creep Properties of Elektron21 Alloy Reinforced by AlN Nanoparticles, Materials 10(12) (2017) 1380.
[11] H. Yang, Y. Huang, S. Gavras, K.U. Kainer, N. Hort, H. Dieringa, Influences of AlN/Al Nanoparticles on the Creep Properties of Elektron21 Prepared by High Shear Dispersion Technology, Jom (2019).
[12] H. Yang, Y. Huang, D. Tolnai, K.U. Kainer, H. Dieringa, Influences of Al and high shearing dispersion technique on the microstructure and creep resistance of Mg-2.85Nd-0.92Gd-0.41Zr-0.29Zn alloy, Materials Science and Engineering: A 764 (2019) 138215.
[13] H. Dieringa, L. Katsarou, R. Buzolin, G. Szakács, M. Horstmann, M. Wolff, C. Mendis, S. Vorozhtsov, D. StJohn, Ultrasound Assisted Casting of an AM60 Based Metal Matrix Nanocomposite, Its Properties, and Recyclability, Metals 7(10) (2017) 388.
[14] H. Yang, Y. Huang, B. Song, K.U. Kainer, H. Dieringa, Enhancing the creep resistance of AlN/Al nanoparticles reinforced Mg-2.85Nd-0.92Gd-0.41Zr-0.29Zn alloy by a high shear dispersion technique, Materials Science and Engineering: A 755 (2019) 18-27.
[15] ASTM E112-13, Standard test methods for determining average grain size, ASTM International, West Conshohocken, PA, 2013.
[16] M. Regev, A. Rosen, M. Bamberger, Qualitative model for creep of AZ91D magnesium alloy, Metallurgical and Materials Transactions A 32(6) (2001) 1335-1345.
[17] J.M.A.P.a.J.P. Abriata, The AI-Zr (Aluminum-Zirconium) System, Phase Diagram Evaluations: Section II 13 (1992) 277-291.
[18] X. He, S. Yang, Y. Du, K. Tao, Y. Fan, Reaction layer formation at the interface between Ti or Zr and AlN, physica status solidi (a) 157(1) (1996) 99-106.
[19] A. Koltsov, F. Hodaj, N. Eustathopoulos, A. Dezellus, P. Plaindoux, Wetting and interfacial reactivity in Ag–Zr/sintered AlN system, Scripta Materialia 48(4) (2003) 351-357.
[20] A. Laik, K. Bhanumurthy, G.B. Kale, Intermetallics in the Zr–Al diffusion zone, Intermetallics 12(1) (2004) 69-74.
[21] W. López-Pérez, R. González-Hernández, J.A. Rodríguez M, Zirconium adsorption and incorporation on a reconstructed Al-T4 AlN(0001) surface, Journal of Physics and Chemistry of Solids 74(10) (2013) 1387-1391.
[22] A.A. Gromov, Y.I. Pautova, A.M. Lider, A.G. Korotkikh, U. Teipel, E.V. Chaplina, T.I. Sigfusson, Interaction of powdery Al, Zr and Ti with atmospheric nitrogen and subsequent nitride formation under the metal powder combustion in air, Powder Technology 214(2) (2011) 229-236.
[23] J. Dai, S. Shen, B. Jiang, J. Zhang, Q. Yang, Z. Jiang, H. Dong, F. Pan, Interfacial reaction in (Mg-37.5Al)/(Mg-6.7Nd) diffusion couples, Metals and Materials International 22(1) (2016) 1-6.

[24] D. Dai, D. Gu, Influence of thermodynamics within molten pool on migration and distribution state of reinforcement during selective laser melting of AlN/AlSi10Mg composites, International Journal of Machine Tools and Manufacture 100 (2016) 14-24.
[25] I. Schmidt, C. Benndorf, Low temperature CVD diamond deposition using halogenated precursors—deposition on low melting materials: Al, Zn and glass, Diamond and related materials 10(3-7) (2001) 347-351.
[26] D. Liu, J. Song, B. Jiang, Y. Zeng, Q. Wang, Z. Jiang, B. Liu, G. Huang, F. Pan, Effect of Al content on microstructure and mechanical properties of as-cast Mg-5Nd alloys, Journal of Alloys and Compounds 737 (2018) 263-270.
[27] H. Dieringa, Y. Huang, P. Wittke, M. Klein, F. Walther, M. Dikovits, C. Poletti, Compression-creep response of magnesium alloy DieMag422 containing barium compared with the commercial creep-resistant alloys AE42 and MRI230D, Materials Science and Engineering: A 585 (2013) 430-438.
[28] Q. Yang, X. Qiu, S. Lv, F. Meng, K. Guan, B. Li, D. Zhang, Y. Zhang, X. Liu, J. Meng, Deteriorated tensile creep resistance of a high-pressure die-cast Mg–4Al–4RE–0.3Mn alloy induced by substituting part RE with Ca, Materials Science and Engineering: A 716 (2018) 120-128.
[29] H. Dieringa, N. Hort, K.U. Kainer, Investigation of minimum creep rates and stress exponents calculated from tensile and compressive creep data of magnesium alloy AE42, Materials Science and Engineering: A 510–511 (2009) 382-386.
[30] Y. LI, T.G. LANGDON, A unified interpretation of threshold stresses in the creep and high strain rate superplacticity of metal matrix composites, Acta Metallurgica 47 (1999) 3395-3403.
[31] P. Zhang, Creep behavior of the die-cast Mg–Al alloy AS21, Scripta Materialia 52(4) (2005) 277-282.
[32] Y. Li, T.G. Langdon, A simple procedure for estimating threshold stresses in the creep of metal matrix conposites, Scripta Materialia 36 (1997) 1457-1460.
[33] N. Mo, Q. Tan, M. Bermingham, Y. Huang, H. Dieringa, N. Hort, M.-X. Zhang, Current development of creep-resistant magnesium cast alloys: A review, Materials & Design 155 (2018) 422-442.
[34] K.R. Athul, U.T.S. Pillai, A. Srinivasan, B.C. Pai, A review of different creep mechanisms in Mg alloys based on stress exponent and activation energy, Advanced Engineering Materials 18(5) (2016) 770-794.
[35] M. Pekguleryuz, M. Celikin, Creep resistance in magnesium alloys, International Materials Reviews 55(4) (2013) 197-217.
[36] S. Gourdet, F. Montheillet, A model of continuous dynamic recrystallization, Acta Materialia 51(9) (2003) 2685-2699.
[37] Y. Shi, L. Luo, Q. Huo, J. Wang, Z. Xiao, J. Guo, X. Yang, Enhancing creep properties of a hot-rolled Mg-4Y binary alloy via a new thought of inhibiting cross-slip, Materials Characterization 147 (2019) 64-71.
[38] Z. Fan, Y. Wang, M. Xia, S. Arumuganathar, Enhanced heterogeneous nucleation in AZ91D alloy by intensive melt shearing, Acta Materialia 57(16) (2009) 4891-4901.
[39] S.J. Liu, G.Y. Yang, S.F. Luo, W.Q. Jie, Microstructure evolution during heat treatment and mechanical properties of Mg–2.49Nd–1.82Gd–0.19Zn–0.4Zr cast alloy, Materials Characterization 107 (2015) 334-342.
[40] L. Peng, P. Fu, Z. Li, Y. Wang, H. Jiang, High cycle fatigue properties of cast Mg–xNd–0.2Zn–Zr alloys, Journal of Materials Science 49(20) (2014) 7105-7115.
[41] Y. Ali, D. Qiu, B. Jiang, F. Pan, M.-X. Zhang, Current research progress in grain refinement of cast magnesium alloys: A review article, Journal of Alloys and Compounds 619 (2015) 639-651.

[42] Y. Tao, G. Ke, Y. Xie, Y. Chen, S. Shi, H. Guo, Adhesion strength and nucleation thermodynamics of four metals (Al, Cu, Ti, Zr) on AlN substrates, Applied Surface Science 357 (2015) 8-13.
[43] Y. Jiang, Y.a. Chen, J. Gao, Comparative study regarding the effect of Al, Zn, and Gd on the microstructure and mechanical properties of Mg alloy Mg-Sn-Li, Materials & Design 105 (2016) 34-40.
[44] F. Kabirian, R. Mahmudi, Effects of Zr additions on the microstructure and impression creep behavior of AZ91 magnesium alloy, Metallurgical and Materials Transactions A 41(13) (2010) 3488-3498.
[45] S.M. Zhu, J.F. Nie, M.A. Gibson, M.A. Easton, P. Bakke, Microstructure and creep behavior of high-pressure die-cast magnesium alloy AE44, Metallurgical and Materials Transactions A 43(11) (2012) 4137-4144.
[46] N. Hort, Y. Huang, K.U. Kainer, Intermetallics in magnesium alloys, Advanced Engineering Materials 8(4) (2006) 235-240.
[47] Y. Ouyang, X. Tao, Y. Feng, Y. Du, X. Zhong, First-principles calculations of elastic constants of DO3-Mg3 RE (RE= Sc, Y, La, Ce, Lu), Physica Scripta 78(6) (2008) 065601.
[48] X. Tao, Y. Ouyang, H. Liu, F. Zeng, Y. Feng, Y. Du, Z. Jin, Ab initio calculation of the total energy and elastic properties of Laves phase C15 Al2RE (RE=Sc, Y, La, Ce–Lu), Computational Materials Science 44(2) (2008) 392-399.
[49] T. Jun, Z.-q. SHI, Creep mechanism and creep constitutive model of aluminum silicate short-fiber-reinforced magnesium matrix composite, Transactions of Nonferrous Metals Society of China 24(3) (2014) 632-640.